



Engineered multi-scale roughness of carbon nanofiller-embedded 3D printed spacers for membrane distillation

Seongeom Jeong^a, Boram Gu^{b,*}, Subi Choi^c, Suk-kyun Ahn^c, Jaegun Lee^d, Jieun Lee^e, Sanghyun Jeong^{a,*}

^a Department of Civil and Environmental Engineering, Pusan National University, Busan 46241, Republic of Korea

^b School of Chemical Engineering, Chonnam National University, Gwangju 61186, Republic of Korea

^c Department of Polymer Science and Engineering, Pusan National University, Busan 46241, Republic of Korea

^d School of Chemical Engineering, Pusan National University, Busan 46241, Republic of Korea

^e Institute for Environment and Energy, Pusan National University, Busan 46241, Republic of Korea

ARTICLE INFO

Keywords:

3D printing
Computational fluid dynamics
Membrane distillation
Roughness
Spacer

ABSTRACT

Membrane distillation (MD) transfers heat and mass simultaneously through a hydrophobic membrane. Hence, it is sensitive to both concentration and temperature polarisation (CP and TP) effects. In this study, we fabricated feed spacers to improve MD efficiency by alleviating the polarisation effects. First, a 3D printed spacer design was optimised to show superior performance amongst the others tested. Then, to further enhance spacer performance, we incorporated highly thermally stable carbon nanofillers, including carbon nanotubes (CNT) and graphene, in the fabrication of filaments for 3D printing. All the fabricated spacers had a degree of engineered multi-scale roughness, which was relatively high compared to that of the polylactic acid (PLA) spacer (control). The use of nanomaterial-incorporated spacers increased the mean permeate flux significantly compared to the PLA spacer (27.1 L/m²h (LMH)): a 43% and 75% increase when using the 1% graphene-incorporated spacer (38.9 LMH) and 2% CNT incorporated spacer (47.5 LMH), respectively. This could be attributed to the locally enhanced turbulence owing to the multi-scale roughness formed on the spacer, which further increased the vaporisation rate through the membrane. Interestingly, only the CNT-embedded spacer markedly reduced the ion permeation through the membrane, which may be due to the effective reduction of CP. This further decreased with increasing CNT concentration, confirming that the CNT spacer can simultaneously reduce the CP and TP effects in the MD process. Finally, we successfully proved that the multi-scale roughness of the spacer surface induces micromixing near the membrane walls, which can improve the MD performance via computational fluid dynamics.

1. Introduction

Membrane distillation (MD), a high-salinity brine water treatment technique, uses a hydrophobic membrane. In this process, the membrane acts as a barrier between the liquid (feed water) and vapour generated by the temperature difference between hot and cold water. It passes through a dry hydrophobic membrane to produce freshwater. The MD process can perfectly (theoretically) reject ions, macromolecules, colloids, and cells (Al-Obaidani et al., 2008; Thomas et al., 2017;

Fortunato et al., 2018). However, this process has not yet been fully commercialised for large-scale industries due to problems that remain to be solved.

During the process of MD, heat and mass are transferred through the hydrophobic membrane; therefore, the process is sensitive to polarisation effects, including both temperature and concentration polarisation (TP and CP) (Martínez-Díez and Vázquez-González 1999; Kuang et al., 2019). TP occurs because of the limited heat transfer in the thermal boundary layer, which is hot side as the feed is in direct contact

Abbreviations: CNT, Carbon nanotubes; CFD, Computational fluid dynamics; CAD, Computer-aided design; CP, Concentration polarisation; DI, Deionised; DCMD, Direct-contact membrane distillation; FFF, Fused filament fabrication; IRE, Ion rejection efficiency; MPF, Mean permeate flux; MD, Membrane distillation; PLA, Polylactic acid; PVDF, Polyvinylidene fluoride; SEM, Scanning electron microscope; TP, Temperature polarisation; 3D, Three-dimensional; 2D, Two-dimensional; WCA, Water contact angle.

* Corresponding authors.

E-mail addresses: boram.gu@jnu.ac.kr (B. Gu), sh.jeong@pusan.ac.kr (S. Jeong).

<https://doi.org/10.1016/j.watres.2023.119649>

Received 19 October 2022; Received in revised form 2 January 2023; Accepted 18 January 2023

Available online 20 January 2023

0043-1354/© 2023 Elsevier Ltd. All rights reserved.

with the membrane (Alsaadi et al., 2014). This results in a lower temperature gradient between membrane surfaces, resulting in a reduction in flux (Manawi et al., 2014). On the feed side, a higher solute concentration in the boundary layer near the membrane surface causes CP (Bahmanyar et al., 2012). This can reduce the flux in the distillation process and further accumulate foulants on the membrane surface, which can lead to membrane fouling or scaling (Chen et al., 2004). Therefore, several researchers have studied methods to enhance MD performance by reducing CP and TP. Hence, advanced membranes (e.g. nanostructured surfaces and metallic membranes) (Kyoungjin An, Lee et al. 2017; Politano et al., 2017; Ragunath et al., 2018; Shukla et al., 2018; Huang et al., 2019; Politano et al., 2019), flow promoters (e.g. feed spacers, corrugated feed channels/membranes, and flashed feed channels) (Phattaranawik et al., 2003; Gurreri et al., 2014; Kharraz et al., 2015; Taamneh and Bataineh 2017; Alsaadi et al., 2018; Elhenawy et al., 2020), and self-heating membranes (e.g. photothermal heating, joule heating, and induction heating) (Dongare Pratiksha, Alabastris et al. 2017; Politano et al., 2017; Politano et al., 2019; Ye et al., 2019; Anvari et al., 2020) have been actively researched to mitigate the TP (Anvari et al., 2020). However, the membranes used in the MD process are difficult to improve because they require several properties: (i) high hydrophobicity, (ii) high permeability, (iii) high mechanical strength, (iv) high thermal stability, (v) high chemical resistance, and (vi) a narrow pore size distribution (Khayet et al., 2005; Lee et al., 2018). Moreover, because the currently developed MD membranes have almost reached the critical point of mass transfer, a significant increase in membrane performance is unlikely with membrane development (Lee et al., 2018). Therefore, many studies have recently focused on flow promoters, such as spacers, in an attempt to improve the MD performance by increasing the convective heat transfer and reducing the TP coefficient in the feed channel (Thomas et al., 2018; Castillo et al., 2019; Tan et al., 2019; Thomas et al., 2019, 2021; Ve et al., 2021; Ni et al., 2022).

Feed spacers are generally used to: (i) separate the membranes, creating channels and (ii) promote fluid mixing in a membrane module. In the MD process, this acts as a promoter of turbulence that disturbs the temperature and concentration boundary layer near the membrane surface, thereby improving membrane performance (Gurreri et al., 2014; Taamneh and Bataineh, 2017). The shape, configuration, diameter, and number of feed spacer filaments have been reported to influence spacer performance (Thomas et al., 2018; Castillo et al., 2019; Thomas et al., 2019, 2021; Ve et al., 2021; Ni et al., 2022). Most currently used spacers are made of low-cost polymeric materials (e.g. polypropylene), and few studies have changed the material of the spacers in the MD process (Table S1) (Ang et al., 2019; Tan et al., 2019; Thomas et al., 2021). In these studies, the spacers were coated with nanoparticles or metals. However, the coating layer peeled off easily during the MD operation, resulting in a reduction in the MD performance. For this reason, research on long-lasting spacers is needed to improve efficiency, even during long-term operation or reuse. Therefore, the method that involves embedding nanoparticles in spacer fabrication is preferred over the coating method.

In recent years, three-dimensional (3D) printing has been widely used in manufacturing to create various designs that cannot be synthesised using conventional technologies (Siddiqui et al., 2016; Castillo et al., 2019; Thomas et al., 2019; Tijing et al., 2020). The advantage of 3D printing technology is its layer-by-layer manufacturing configuration. This makes it easy to create almost any complex geometry at different scales, which enables the rapid creation of finished goods (Bogue, 2013; Attaran, 2017). 3D printing uses a wide variety of materials, such as plastics, resins, rubbers, ceramics, glass, concrete, and metals. Fused filament fabrication (FFF) 3D printers are widely used because they can print most filament-type thermoplastic materials.

Using this technology, this study aimed to create a nanofiller-embedded spacer that can easily embed nanofillers into filaments by simple mixing (Lee et al., 2016). Amongst the many candidate

nanofillers, we tested two classes of carbon nanomaterials: carbon nanotube (CNT) and graphene. These are interesting candidates for use as additives in spacers because they exhibit high thermal and electrical conductivities and mechanical strengths. However, graphene has a two-dimensional (2D) structure and CNT has a 3D structure. Compared to flat structured graphene, CNT do not disperse well due to their cylindrical structural characteristics; therefore, it is expected to have different effects on the improvement of MD performance by spacers. For these reasons, we hypothesise that embedding carbon nanofillers can strongly improve the material properties of weak plastic spacers, reduce the polarisation effects, and improve the MD process performance. In addition, CNT and graphene show different mechanisms in the spacer.

The objective of this study was to increase the MD efficiency using carbon nanomaterial-embedded spacers and to investigate their mechanisms in MD performance enhancement. Herein, we provide an easy approach for fabricating nanofiller-embedded spacers using an FFF-3D printer. To evaluate this hypothesis, the impact of embedding nanofillers on a 3D printed spacer surface, namely on morphology, hydrophobicity, and surface roughness, was examined using an optical microscope, scanning electron microscope (SEM), contact angle, and 3D laser microscope. We then performed direct-contact membrane distillation (DCMD) to specifically evaluate the efficiency of unembedded and embedded nanofiller spacers with the same geometry. Next, computational fluid dynamics (CFD) was used to investigate the hydrodynamics and heat and mass transfer within a spacer-filled feed channel depending on the spacer type to elucidate the performance discrepancy between the different spacers used in this study.

2. Materials and methods

2.1. Feed spacer

2.1.1. Filaments

In this study, the 3D printing filaments used were commercial filaments for a poly lactic acid (PLA) spacer and fabricated filaments for nanofiller-embedded spacers using a filament extruder (Filibot H400; Fordentech, Republic of Korea). To prepare the nanofiller-embedded filaments, poly lactic acid (PLA) pellets (PLA Pellet; Total Corbion, Netherlands) were mixed with carbon nanofillers including CNT (BT1003M; LG Chemical, Republic of Korea) and graphene (Sigma-Aldrich, USA) by shaking several times together in a bottle. Subsequently, a well-mixed pellet containing carbon nanofillers was injected into the filament extruder. Filaments were produced at 230–250 °C: 250 °C for the CNT filament and 230 °C for the graphene filament.

2.1.2. 3D printed feed spacer

We produced feed spacer designs using the Fusion 360 version 2020 computer-aided design (CAD) software (Autodesk, CA, USA). To optimize the feed spacer design, we varied the angle of feed spacer (crossing angle of the filament) to 45° and 90°, the thickness of spacer to 0.5, 0.7, and 1.0 mm and the arrangement of filament interval to 1, 2, 3, and 4 mm. The designs were 3D printed using a fused filament fabrication (FFF) 3D printer (Ender-3 pro; Creality, China). All of the spacers were printed at a size of 10 × 4 cm, and then cut to 6.0 × 1.5 cm for MD operation.

2.1.3. Characterization of spacer

To observe the morphology of the spacer, an optical microscope (DN-10A; Samwon Scientific, Republic of Korea) was used. Using the optical microscope, the surface of the spacer was examined without any treatment and images of the spacer surface were captured at a magnification of 100×. A laser scanning confocal microscope (OLS 5000; Olympus, Japan) was used to obtain the three-dimensional morphology and measure the multiscale roughness of the spacer surface. The surface roughness was reported as the average value of R_a values of six readings taken at different points on the spacer surface at a magnification of 5×.

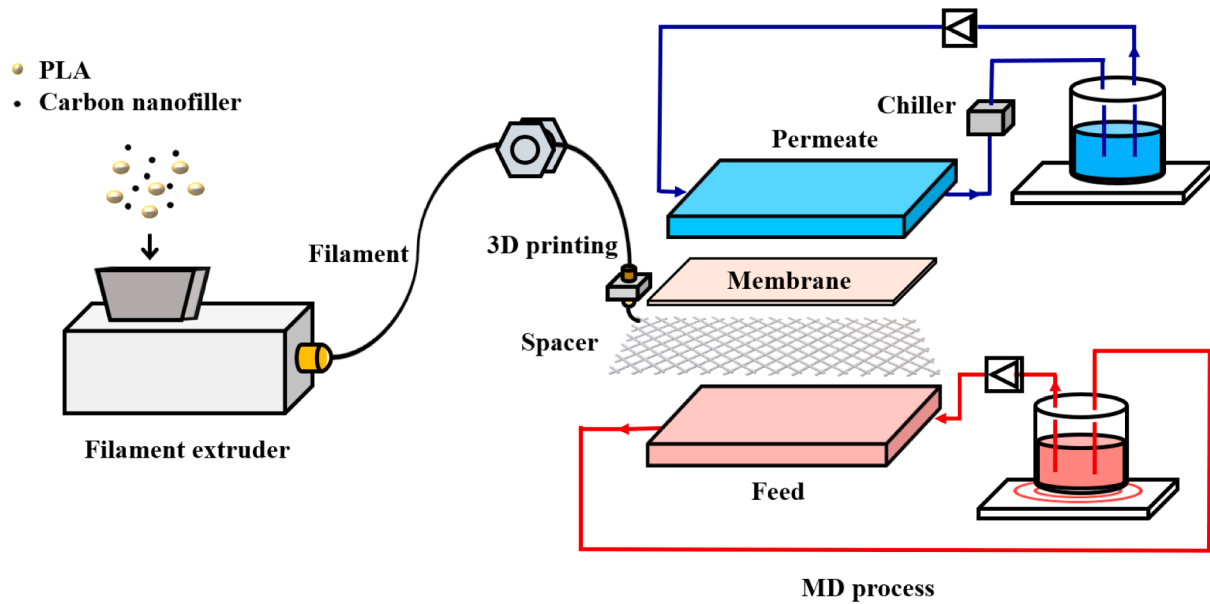


Fig. 1. A schematic diagram of MD operation with 3D printed carbon nanofiller embedded spacers.

The hydrophobicity of the spacer was tested using a contact angle analyser (phoenix10; SEO, Republic of Korea). The water contact angle (WCA) was determined using a 1- μ L deionised (DI) water droplet on a spacer filament using a micropipette. The reported WCA measurements represent the average of five readings taken at different locations on the sample to ensure values representative of the entire sample.

As reported by Li et al. (2021), the relationship between WCA and surface roughness was analysed using the Cassie-Baxter equation. The equation is taken from previous studies (Ramiasa et al., 2014; Wang et al., 2020):

$$\cos\theta^{real} = f_1(\cos\theta^{SS} + 1) - 1$$

where θ^{real} is the contact angle of the Cassie contact angle and θ^{SS} is the contact angle of the smooth surface. When the f_1 (solid on surface fraction) is less than 1, the measured surface is called the established Cassie-Baxter surface.

2.2. Direct contact membrane distillation (DCMD) experimental set-up

The MD module was composed of poly-(methyl methacrylate) plastic, and the module channel dimensions were $0.015 \times 0.065 \times 0.002$ m ($L \times W \times H$). The MD tests were performed using a 0.22- μ m

polyvinylidene fluoride (PVDF) (Durapore®, Germany) hydrophobic membrane. The main characteristics of the MD membranes are summarised in Table S2.

The feed was comprised of a solution of 35 g/L sodium chloride (NaCl, Daejung, Republic of Korea), which was prepared by dissolving 35 g/L NaCl in DI water.

Fig. 1 shows the laboratory-scale DCMD setup. The feed temperature was maintained at 60 °C using a hot plate (RCT basic; IKA, Germany) with a temperature sensor (PT 1000.60; IKA, Germany). The permeate temperature was maintained at 19.5 ± 0.5 °C by using a chiller (RW3-0525; Jeio Tech, Republic of Korea). The feed solution was continuously stirred using a magnetic stirrer to prevent the feed solution from crystallisation and sedimentation. The weight of the permeate was recorded on a computer every minute using an electronic balance (PR4202KR/E; Ohaus, USA). The flow rates of both the feed and permeate solution sides were controlled at 0.5 L/min (LPM) using two gear pumps (EMS-4000; EMS Tech, Republic of Korea). Before starting the MD test, DI water was circulated for 30 min to stabilise the flux. All MD tests were operated for 1-h using 35 g/L NaCl feed solution. The conductivity of the permeate water was measured using a conductivity metre (HI9033; HANNA® Instruments, USA) to measure the ion rejection efficiency (IRE). Our measured the feed conductivity was 65.0 mS/cm at 60 °C (62.4 mS/cm at 20 °C). After completing the test, the

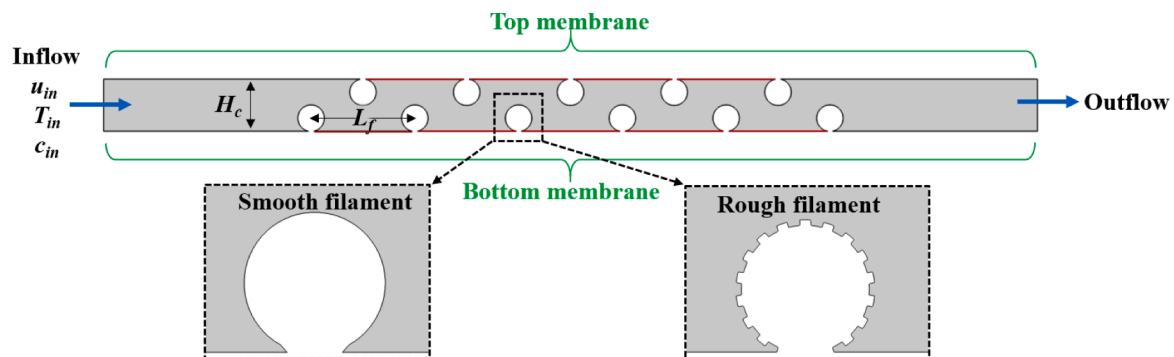


Fig. 2. Illustration of smooth and rough spacers within a fluid domain for a 2D feed channel along with a brief description of boundary conditions. Membrane areas coloured in red were analysed for water and salt fluxes and wall concentrations and temperature for minimal entrance and exit effects, although permeation boundary conditions are applied for the entire top and bottom membrane areas. (For interpretation of the references to colour in this figure legend, the reader is referred to the web version of this article.)

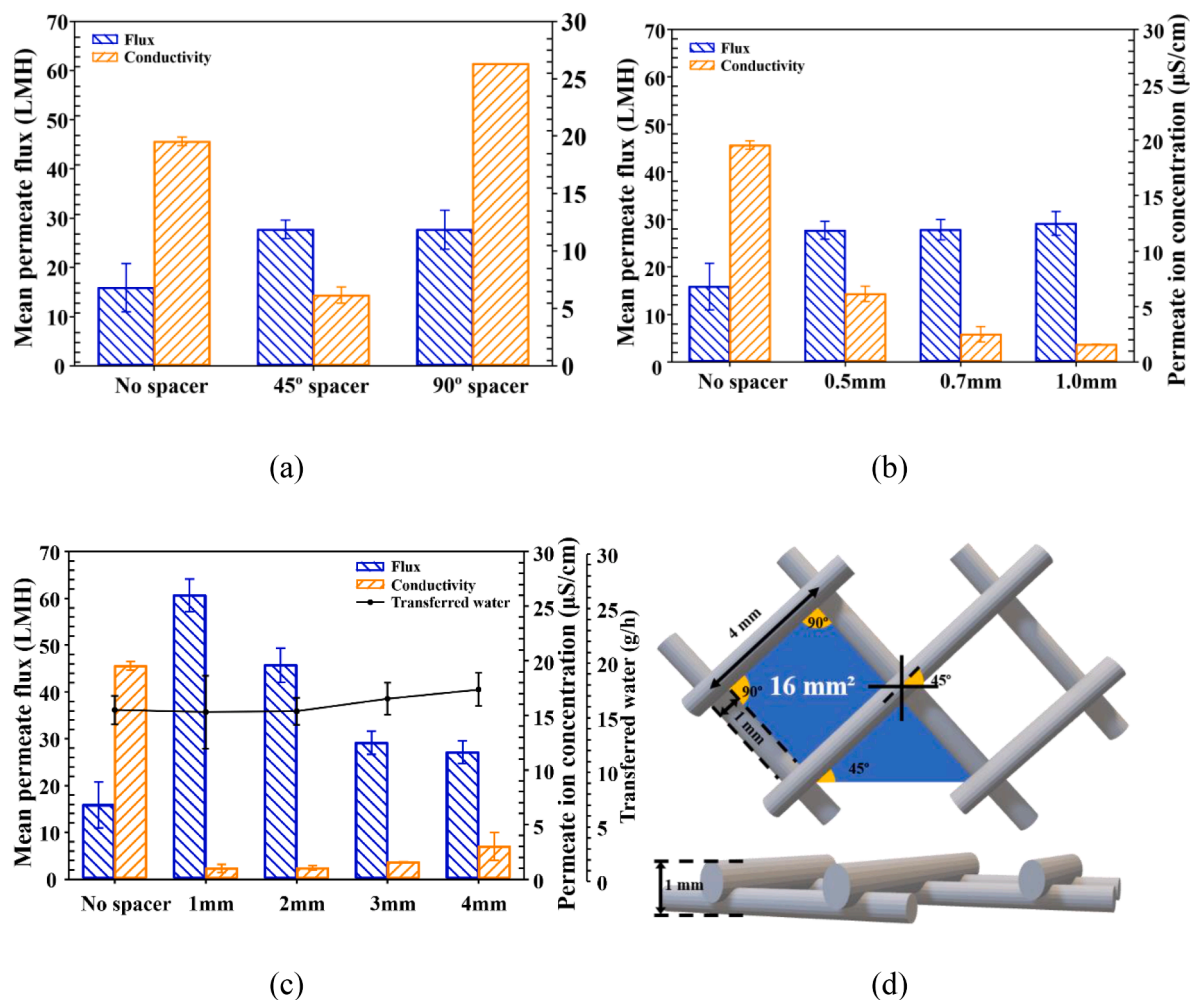


Fig. 3. MD performance (MPF and IRE) with different feed spacers fabricated at varied factors: (a) crossing angle of the spacer filament, (b) thickness of spacer, (c) arrangement interval of the filament, and (d) optimized design of spacer. (Operating conditions: inlet feed and permeate flow rates of 0.5 LPM and inlet feed and permeate temperatures of 60 °C and 19.5 °C, respectively).

conductivity of the feed solution and permeate water was measured to check the penetration of ions from the feed to the permeate side. All tests were repeated at least three times. The IRE was calculated as the increase in the permeate ion concentration over time. Permeate flux J (L/m²h, LMH) was calculated using the following equation:

$$J = \frac{Q}{A \times t}$$

where Q is the permeated water volume (L), A is the effective area of the membrane (m²), and t is time (h).

2.3. Multiphysics simulation of a spacer-filled feed channel in DCMD

Computational simulations were performed to investigate the fluid dynamics and heat and mass transfer within a 2D feed channel for the MD. Steady-state simulations for laminar, incompressible, and Newtonian flows were performed under a wide range of water and salt permanence parameters. An aqueous NaCl solution was selected as the feed solution, which was similar to the experimental feed solution. Fig. 2 illustrates the fluid domain of the 2D MD feed channel, where several circular filaments are directly in contact with semi-permeable membrane walls with an even spacing of L_f . The filament radii are half of the channel height H_c , so that the two layers of filaments tightly fit the channel height. The entrance and exit of the feed stream are placed $2L_f$ away from the first and last filaments at the bottom. From the

experimental measurements (shown in the next section), the major morphological feature of CNT-embedded spacers differentiated from PLA spacers was found to be surface roughness. Because it is difficult to realistically mimic the observed surface morphology of the rough CNT-embedded spacers, a cogwheel shape was assumed to represent the rough CNT-embedded spacers instead, with the height of the teeth being the surface roughness measured in the experiments (44 μm was chosen to represent the roughest filaments).

To reduce the computational burden, we omitted a permeate channel because it can be assumed that the permeate concentration and temperature remain relatively constant along the channel compared to those in the feed channel because of the high salt rejection and direct condensation in DCMD. Nonetheless, water and salt fluxes through membranes, which are dependant on the differences in vapour pressures and salt concentrations between the feed and permeate sides, can be considered via the mechanistic model of water vapour and salt permeation imposed at the membrane wall boundaries. The mathematical expressions of water and salt fluxes were prescribed at the top and bottom membranes so that permeating water and salt fluxes could be calculated as a function of the wall temperature and concentration. A constant flow velocity (u_{in}), NaCl concentration (c_{in}), and temperature (T_{in}) were imposed at the inlet of the 2D channel. The walls of the spacer filaments were assumed to be non-slip and insulated. Details of the governing equations for momentum, heat and mass transfer, and boundary conditions can be found in Section A.2 of the Supporting

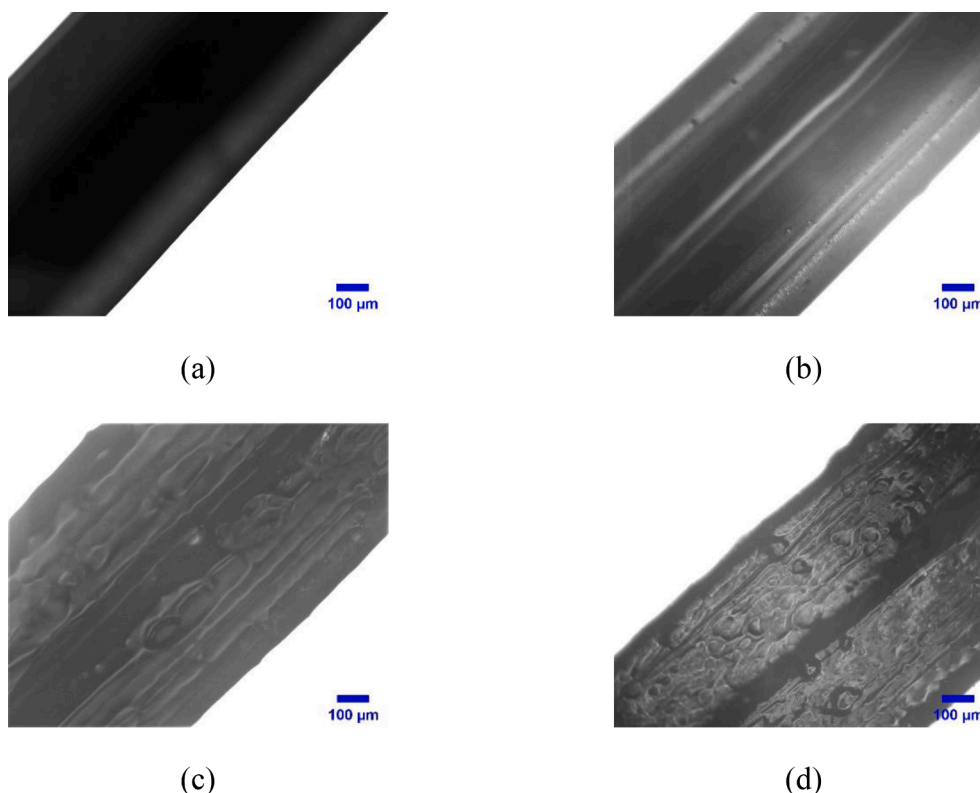


Fig. 4. Optical microscope images (100 \times) on the surfaces of (a) PLA spacer, (b) 1% graphene spacer, (c) 1% CNT spacer, and (d) 2% CNT spacer.

Information, along with the simulation conditions and computational setup. The simulation conditions were chosen based on the experimental setup in this work and the membrane properties in existing studies (Table S4 in the Supporting Information).

3. Results and discussion

3.1. Spacer design optimization

In this study, spacer design was optimised based on mean permeate flux (MPF) and ion rejection efficiency (IRE). Three different factors were considered for 3D printed PLA spacers: (i) crossing angle of the spacer filament, (ii) spacer thickness, and (iii) arrangement interval of the filament. Fig. 3 shows the MPF and IRE of the MD tested with differently fabricated feed spacers. As expected, MPF and IRE with spacers were higher than those without spacers owing to the reduction of CP and TP on the membrane surface.

3.1.1. Crossing angles of spacer filament

Fig. 3(a) shows the MPF and permeate ion concentrations according to the crossing angles of the spacer filament. Fig. S1 compares the designs of 90° and 45° spacers. The crossing angles of the spacer filaments did not affect MPF. However, the permeate ion concentration with the 45° spacer was much lower than that with the 90° spacer. This indicates that compared to the 90° spacer, the 45° spacer significantly disrupted the CP on the membrane surface, resulting in better IRE. In 45° spacer than 90° spacer, flow velocity is faster and a lot of turbulence is formed, which improved IRE (Alsaadi et al., 2014).

3.1.2. Thickness of spacer

As shown in Fig. 3(b), MPF increased with increasing the thickness of spacer from 0.5 mm to 1.0 mm. The permeate ion concentration was also lower with thicker spacers (0.5 mm to 1.0 mm). This implies that thicker spacers (0.5 mm to 1.0 mm) resulted in less CP. This is because thicker

spacer can generate more turbulence near the membrane surface than thinner spacer owing to larger contact area with feed water. Therefore, the IRE improvement of thicker spacers (0.5 mm to 1.0 mm) implies that thicker spacers were able to reduce the CP by forming more turbulence and reducing the thickness of boundary layer.

3.1.3. Arrangement interval of the filament

The MD performance according to the spacer filament arrangement interval (1–4 mm) is shown in Fig. 3(c). The effective area of the membrane was smaller with a narrower spacer filament arrangement interval. Therefore, a spacer with a wider arrangement interval of the filament resulted in a higher transfer of water, while a spacer with a narrower arrangement interval of the spacer filaments presented a higher MPF. In contrast, the permeate ion concentration increased as the spacer filament arrangement interval increased. This indicates that the narrow arrangement interval of the spacer filaments creates a large amount of turbulence and transfers a small amount of water, but controls the CP well. In this study, the 4 mm spacer was chosen as the best design as the narrow arrangement interval of the filament was more expensive and resulted in a lower degree of water penetration.

The optimal spacer design was chosen in terms of a high MPF, low permeate ion concentration, high water production, and low fabrication cost. Similarly, a CFD study of spacer geometries by Yazan et al. reported that a crossing angle of 45° exhibited the best performance (Taamneh and Bataineh, 2017). Therefore, the optimal spacer design is a 45° crossing angle of the spacer filament, 1.0 mm thickness of spacer, and 4 mm arrangement interval of the filament (Fig. 3(d)). This design has been continuously used for the fabrication of other feed spacers.

3.2. Change in spacer surface

3.2.1. Morphology of spacer

Fig. 4 shows the surface morphology difference of spacers before and after adding nanofillers (e.g. graphene, CNT). The surface of the PLA

Table 1

Water contact angle and surface roughness of carbon nanofiller embedded spacers.

	PLA	0.5% CNT	1% CNT	2% CNT	0.5% graphene	1% graphene
WCA (°)	65.0 (±0.2)	71.9 (±0.4)	72.3 (±2.0)	96.4 (±3.4)	71.8 (±1.3)	75.2 (±2.9)
f_1 (Cassie-Baxter equation)	1.00	0.92	0.91	0.62	0.93	0.88
Roughness (μm)	13.5 (±1.9)	12.2 (±7.2)	25.2 (±12.6)	44 (±18.2)	5.0 (±1.3)	5.3 (±3.9)

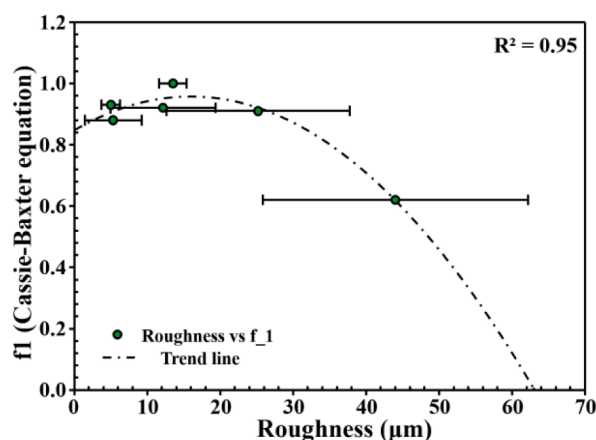
spacer was relatively smooth (Fig. 4(a)), the 1% graphene spacer also presented smooth surface (Fig. 4(b)). However, the 1% CNT spacer (Fig. 4(c)) showed a greatly rougher structure than the PLA or 1% graphene spacers. Fig. 4(d) shows the surface of the 2% CNT spacer, which had the bumpiest and roughest surface amongst the spacers fabricated. As reported by Ngoma et al., the surface became roughest at high CNT concentrations because of the aggregation effects, which is a common feature of the CNT (Ngoma et al., 2021).

3.2.2. Surface roughness and hydrophobicity of spacer surface

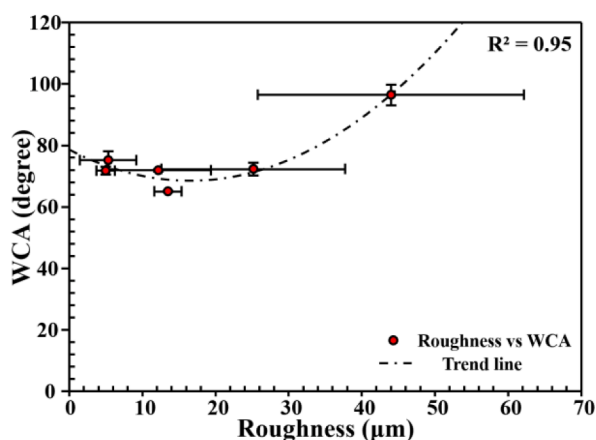
Table 1 shows the relationship between the roughness and WCA of

spacers fabricated under different conditions. The order of measuring WCA of all the carbon nanofillers embedded spacers surface; 2% CNT spacer ($96.4 \pm 3.4^\circ$) > 1% graphene spacer ($75.2 \pm 2.9^\circ$) > 1% CNT spacer ($72.3 \pm 2.0^\circ$) > 0.5% CNT spacer ($71.9 \pm 0.4^\circ$) > 0.5% graphene spacer ($71.8 \pm 1.3^\circ$) > PLA spacer ($65.0 \pm 0.2^\circ$). The WCA of 2% CNT embedded 3D printed spacer increased sharply to 96.4° , indicating that surface hydrophobicity was increased greatly by the CNT aggregation effects on the spacer surface.

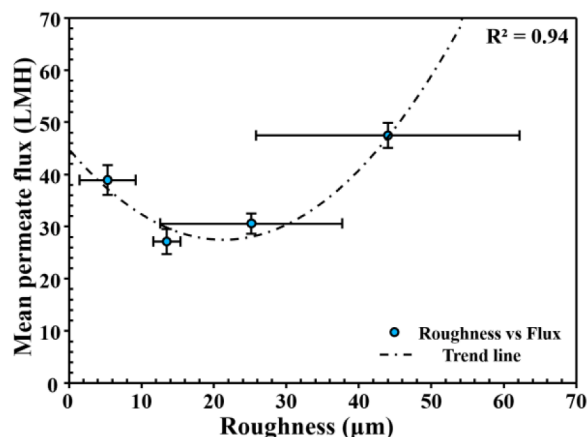
Based on the measured WCA, the Cassie-Baxter equation was calculated, where θ^{real} is the WCA for the carbon nanofiller-embedded spacers and θ^{SS} is the WCA of the PLA spacer. The calculation indicated that all carbon nanofiller-embedded spacers' f_1 was below 1. Therefore, the carbon nanofiller-embedded spacers are the Cassie-Baxter surface. In the PLA spacer, f_1 was 1. The 2% CNT spacer exhibited the lowest f_1 of 0.62. The 0.5% and 1% CNT spacers and 0.5% graphene spacer had similar f_1 values, namely 0.92, 0.91, and 0.93, respectively. The f_1 of 1% graphene spacer was 0.88. A decrease in f_1 indicates that the trapped air ratio at the surface increases and the surface density decreases, indicating that the roughness increases (Wang et al., 2020). Therefore, according to Cassie-Baxter equation, the roughness of the spacers was as follows: 0.5% graphene spacer \leq 0.5% CNT spacer \leq 1% CNT spacer < 1% graphene spacer << 2% CNT spacer. This implies that if the concentration of each carbon nanofiller increases, the roughness increases; in particular, the roughness of 2% CNT spacer will be higher



(a)



(b)



(c)

Fig. 5. Relationships between (a) the roughness and f_1 , (b) the roughness and WCA on the spacer surface, and (c) the roughness and MPF.

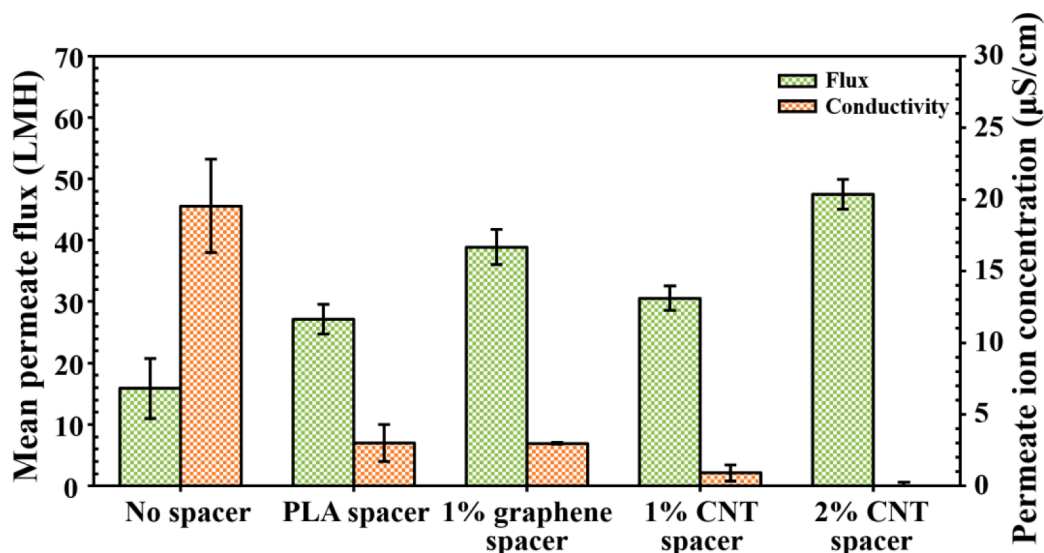


Fig. 6. Effect of spacers on MPF and IRE (in terms of permeate ion concentration). (Operating conditions: feed solution = 35 g/L NaCl, inlet feed and permeate flow rates of 0.5 LPM and inlet feed and permeate temperatures of 60 °C and 19.5 °C, respectively).

than that of the other spacers.

According to the results of the measured surface roughness of the spacers, the 2% CNT embedded spacer showed the highest micro-scale surface roughness ($44 \pm 18.2 \mu\text{m}$) compared to PLA spacer without nanofillers ($13.5 \pm 1.9 \mu\text{m}$). As can be seen from the optimal microscope image of 2% CNT spacer (Fig. 4(d)), a bumpy micro-morphological pattern was observed on the surface. This means that the CNT aggregation occurring at a concentration of CNT over 2% affects the bumpy roughness of the spacer surface. In addition, the 1% CNT spacer and the 2% CNT spacer showed high standard deviations of $12.6 \mu\text{m}$ and $18.2 \mu\text{m}$, respectively, indicating that the 1% and 2% CNT spacers had multi-scale roughness of varying degrees. The graphene-embedded spacers showed a roughness standard deviation similar to that of the PLA spacer. However, micro-scale roughness increased in the following order: 1% CNT spacer ($25.2 \pm 12.6 \mu\text{m}$) > 0.5% CNT spacer ($12.2 \pm 5.3 \mu\text{m}$) > 1% graphene spacer ($5.3 \pm 3.9 \mu\text{m}$) > 0.5% graphene spacer ($5.0 \pm 1.3 \mu\text{m}$). In here, CNT with 3D particle structure showed a rough surface due to aggregation, but graphene with 2D structure was well dispersed and no surface change.

Fig. 5(a) shows the correlation between surface roughness and f_1 . As previously stated, in practice, the lower f_1 , the higher the roughness of the spacer surface. This means that embedding carbon nanofillers in the spacer results in multi-scale roughness owing to the addition of carbon nanofillers forming a Cassie-Baxter surface on the spacer surface. In addition, the values of WCA tended to be similar to those of roughness, and the higher the roughness, the higher the WCA (Fig. 5(b)). The spacer hydrophobicity was the highest when the roughness on the spacer increased to $44 \pm 18.2 \mu\text{m}$. This indicates that embedding carbon nanofillers in the spacer increases the surface roughness by increasing the trapped air ratio on the surface. Furthermore, it increases the hydrophobicity of the spacer surface (Fig. 5(b)). Therefore, surface roughness plays a key role in determining the hydrophobicity of the spacer surface.

3.3. Performance of rough spacers

3.3.1. MD efficiency depending spacer roughness

The use of a spacer increased the MPF compared to MD operation without a spacer (Fig. 6). Then, the use of carbon nanofiller-embedded spacers was found to result in an improved MPF compared to the use of the PLA spacer. In the absence of a spacer (only membrane), MPF was $15.9 \pm 4.9 \text{ LMH}$. The PLA spacer ($27.1 \pm 2.4 \text{ LMH}$) resulted in a 171%

increase in MPF compared to no spacer. This means that spacers promote fluid mixing in the membrane module (Taamneh and Bataineh, 2017), thereby increasing the efficiency of the MD process. The 1% graphene spacer achieved an MPF of $38.9 \pm 2.8 \text{ LMH}$, which is 143% more than the PLA spacer. Furthermore, 1% and 2% CNT spacers achieved better MPF performances than the PLA spacer (113% and 175% higher, respectively). The 2% CNT spacer showed the best performance, with the highest MPF of $47.5 \pm 2.4 \text{ LMH}$. The order of MPF was as follows: 2% CNT spacer ($47.5 \pm 2.4 \text{ LMH}$) > 1% graphene spacer ($38.9 \pm 2.8 \text{ LMH}$) > 1% CNT spacer ($30.6 \pm 2.0 \text{ LMH}$) > PLA spacer ($27.1 \pm 2.4 \text{ LMH}$) > no spacer (only membrane, $15.9 \pm 4.9 \text{ LMH}$). In terms of surface roughness (Table 1), MPF performance tended to be similar with the surface roughness (2% CNT spacer > 1% graphene spacer > 1% CNT spacer > PLA spacer) of the spacer (Fig. 5(c)). The reason why the rough surface spacer made the higher flux is that the rough surface interrupted feed flow and created turbulence. If the flow velocity near the membrane surface is increased by turbulence generated on rough surface, the flux can be improved. This indicates that a rougher surface spacer could improve the MPF performance in the MD process and suggests that a rough spacer surface can cause more turbulence and improve the efficiency of the MD process. In addition, a suitable roughness is expected to increase the efficiency further.

Moreover, the use of a spacer was found to enhance the IRE, presumably owing to the reduction in CP (Fig. 6). The permeate ion concentration was found to decrease in the following order: no spacer (only membrane used, $19.54 \pm 3.3 \mu\text{S/cm}$) >> PLA spacer ($3.0 \pm 1.3 \mu\text{S/cm}$) > 1% graphene spacer ($2.97 \pm 0.1 \mu\text{S/cm}$) > 1% CNT spacer ($0.9 \pm 0.6 \mu\text{S/cm}$) > 2% CNT spacer ($-0.13 \pm 0.4 \mu\text{S/cm}$). IRE was above 97% when spacers were used; however, it is impossible to operate for a long time without controlling the CP. The CP must be controlled in the MD process because it allows for long-term operation without membrane contamination and increases the life of the membrane. CP causes membrane wetting and a high concentration near the membrane surface, and feed water passes through the membrane, reducing the IRE. Therefore, the CP is related to the IRE. Graphene embedded spacer had relatively smooth surface while CNT embedded spacer had bumpy surface as CNT showed aggregation effects (Fig. 4), which is probably due to their different dispersion states. This study showed that the CNT-embedded spacer with multi-scale roughness increased both MPF and IRE, but the change in physical properties and increase in hydrophobicity due to graphene, increase the MPF but not IRE. Since graphene and CNTs share the same chemistry, we consider that both graphene and

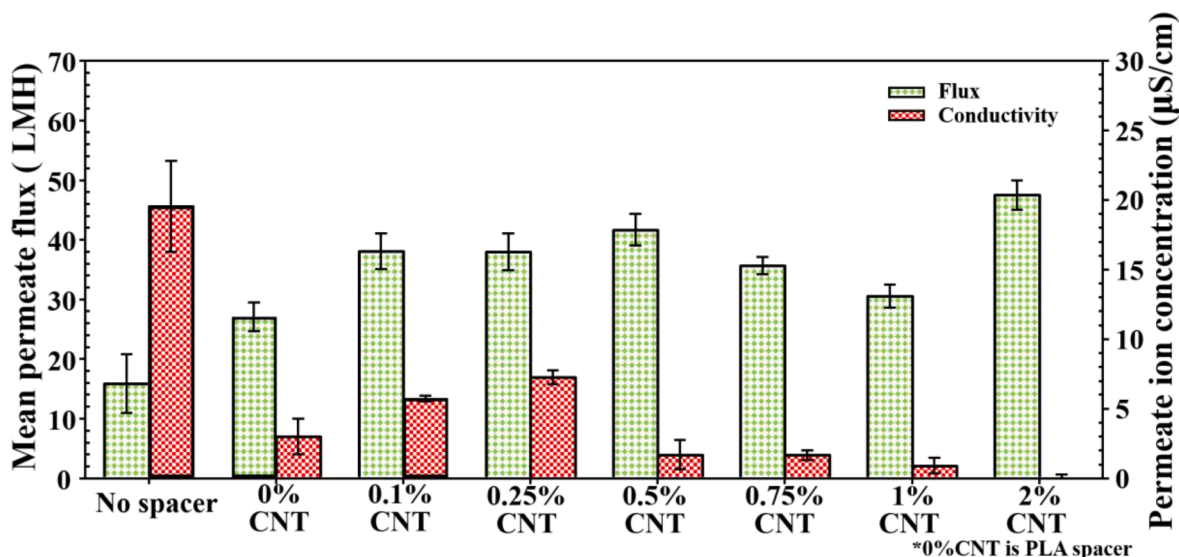


Fig. 7. MD performance in terms of MPF and ion rejection tested with spacers fabricated at different CNT concentrations. (Operating conditions: feed solution = 35 g/L NaCl, inlet feed and permeate flow rates of 0.5 LPM and inlet feed and permeate temperatures of 60 °C and 19.5 °C, respectively) (*0% CNT denotes the PLA spacer).

Table 2

The MPF, surface roughness and WCA of CNT embedded spacer.

	PLA	0.1% CNT	0.25% CNT	0.5% CNT	0.75% CNT	1% CNT	2% CNT
MPF (LMH)	27.1 (±2.4)	38.1 (±3.0)	38.0 (±3.1)	41.7 (±2.6)	35.7 (±1.5)	30.6 (±2.0)	47.5 (±2.4)
WCA (°)	65.0 (±0.2)	65.4 (±0.4)	66.3 (±0.5)	71.9 (±0.4)	72.7 (±0.2)	72.3 (±2.0)	96.4 (±3.4)
Roughness (µm)	13.5 (±1.9)	9.5 (±4.8)	12.3 (±5.3)	12.2 (±7.2)	12.3 (±2.5)	25.2 (±12.6)	44 (±18.2)

CNT embedded spacers should have similar characteristics except surface roughness. So, these results indicate that an increased spacer surface roughness promotes membrane surface turbulence and convective mass transfer near the membrane surface. As reported by the previous study (Lee et al., 2018), high flow velocity increased MPF and reduced polarization effects due to increased local mass transfer near the membrane surfaces. This suggests that only the CNT-embedded spacer can control the CP effect during the MD process. Our results are consistent with the reported findings that the rough surface spacers exhibit high local velocity and consequently enhanced convective mass transfer, thereby mitigating the polarization effects and improving the MPF and IRE.

3.3.2. Effect of CNT spacer on MD performance

Fig. 7 shows the MPF and permeate ion concentration in the MD operation using spacers fabricated at different CNT concentrations. MPF was found to increase as the CNT concentration increased from 0 to 0.5%. Then, the MPF of the spacer of 0.5–1% CNT concentration seemed to decrease as the CNT concentration increased. However, the 2% CNT spacer achieved the highest MPF.

Fig. 7 shows the MPF and permeate ion concentration in the MD operation with spacers fabricated at different CNT concentrations. The MPF increased as the CNT concentration increased from 0 to 0.5%. Then, the MPF of the spacer embedded 0.5–1% CNT concentration seemed to decrease as the CNT concentration increased. However, the 2% CNT spacer achieved the highest MPF.

Permeate ion concentration seemed to increase as the concentration of CNTs increased from 0 to 0.25%, but decreased as the concentration of CNTs increased from 0.25 to 2%. Complete ion rejection was achieved with the 2% CNT. Overall, the IRE increased as a function of the CNT concentration. This indicates that the CNT-containing spacer effectively reduced the CP effect.

Table 2 shows the MPF, WCA, and roughness as a function of CNT

concentration. Overall, both the WCA and roughness increased as the CNT concentration increased. In particular, the higher the CNT concentration, the higher the standard deviation of the spacer surface roughness. This means that CNT promotes multi-scale roughness by creating different roughness sizes on the spacer surface. Multi-scale roughness refers to roughness on various scales from micro to nano, so it appears high standard deviation. It creates irregular turbulences and some of them forms high voltage turbulence. It increases flow rate nearby membrane surface and reduces polarization effects due to reducing of boundary layer. Consequently, multi-scale roughness can improve MRF. In our results, the MPF increased as the roughness increased but decreased at some CNT concentrations. The 0.25–0.75% CNT spacer showed no difference in the roughness, but only a change in the standard deviation of the roughness. However, the 0.75% CNT spacer had a smaller standard deviation of roughness than the 0.25% and 0.5% CNT spacers, corresponding to a lower MPF. In particular, WCA and the roughness of the 2% CNTs increased suddenly with a high standard deviation of roughness. This is in agreement with the highest MPF of 2% CNT spacer, and indicates that the enhancement in MPF can be mainly attributed to the increased multi-scale roughness.

3.4. Computational fluid dynamics (CFD)

3.4.1. Average water and salt fluxes under a range of water and salt permeances

Fig. 8 shows average water and salt fluxes for the membrane area (coloured in red in Fig. 2) over a wide range of water and salt permeances. Fig. 8(a) and (b) shows the results of simulations with varied water permeance (0.5×10^{-7} to 2.0×10^{-6} kg/(m²·s·Pa)) and fixed salt permeance (1×10^{-10} m/s). When evaluating the differences between the CNT-free and CNT-embedded spacers, it was hypothesized that surface roughness would affect the micro-hydrodynamics near the membrane surfaces, leading to enhanced micro mixing that can mitigate

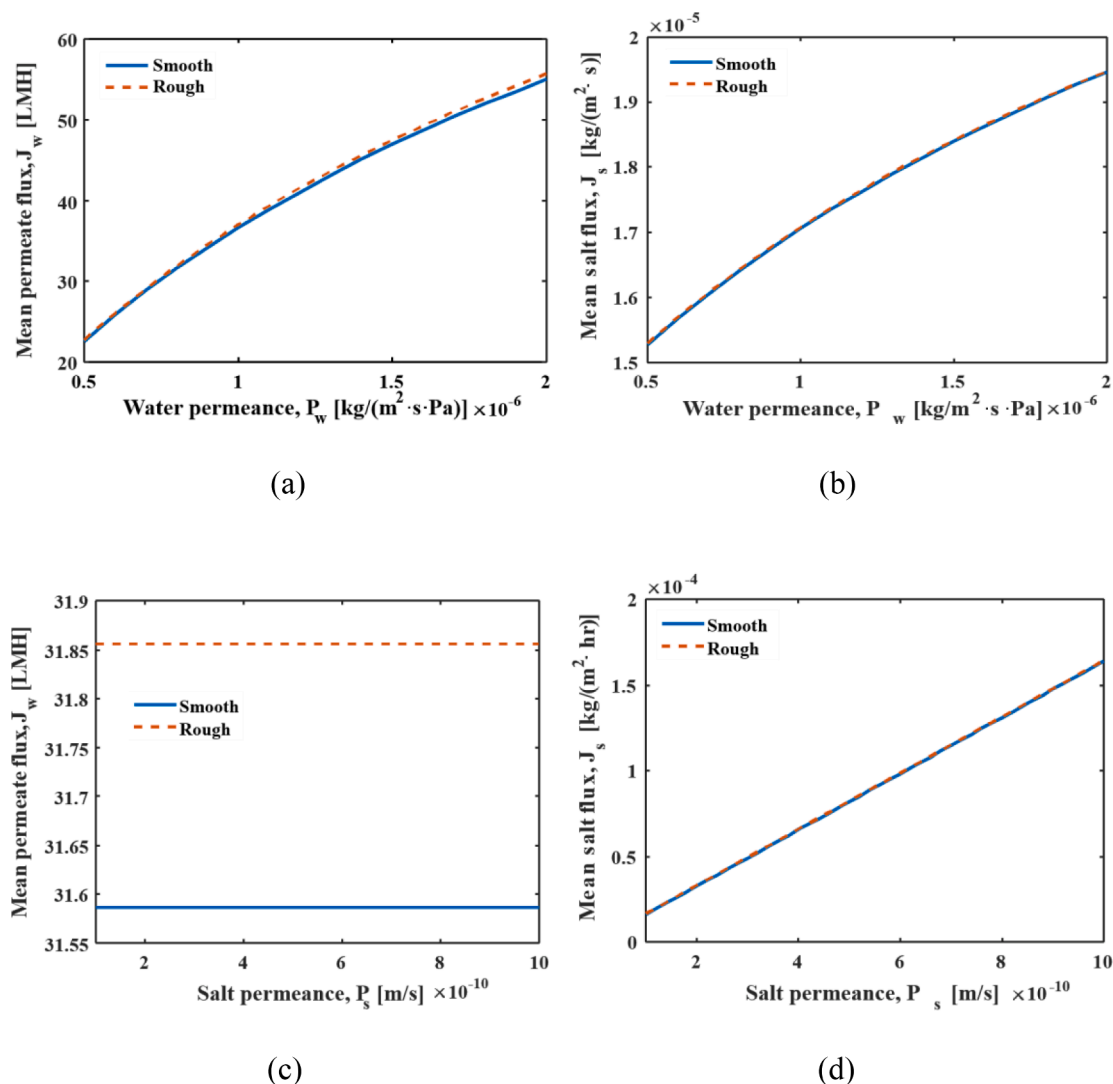


Fig. 8. Simulation results of averaged fluxes and permeate concentrations for varied water and salt permeances. (a) Average water flux and (b) salt flux for varied water permeance (0.5×10^{-7} to $2.0 \times 10^{-6} \text{ kg}/(\text{m}^2 \cdot \text{s} \cdot \text{Pa})$) and fixed salt permeance ($1 \times 10^{-10} \text{ m/s}$) and (c) average water flux and (d) salt flux for fixed salt permeance ($8 \times 10^{-7} \text{ kg}/(\text{m}^2 \cdot \text{s} \cdot \text{Pa})$) and varied salt permeance ($1 \times 10^{-10} \text{ m/s}$ to $1 \times 10^{-9} \text{ m/s}$).

TP. This hypothesis was made based on the experimental observations shown in Table 2. At high CNT concentrations of $>1\%$, a marked increase in surface roughness and mean water flux was observed. On the other hand, at low CNT concentrations, surface roughness and mean water flux did not exhibit distinct trends after considering the measurement errors.

As shown in Fig. 8(a) and (b), the average water flux increased from approximately 22 to 55 LMH for both smooth and rough spacers. In contrast, the salt fluxes did not exhibit a marked variation with an increased water permeance (i.e., $1.5 \times 10^{-5} \text{ kg}/(\text{m}^2 \cdot \text{h})$ to $1.9 \times 10^{-5} \text{ kg}/(\text{m}^2 \cdot \text{h})$). This is because the main driving force of water permeation through membranes in DCMD is the difference in vapour pressure between the feed and permeate streams derived from the temperature gradients. A slight increase in the calculated salt fluxes with increasing water permeance was attributed to the CP aggravated by the enhanced water flux. PLA spacers achieved approximately 30 LMH (Fig. 6), which can be equivalently achieved with a water permeance of 7×10^{-6} to $8 \times 10^{-6} \text{ kg}/(\text{m}^2 \cdot \text{s} \cdot \text{Pa})$. The average water fluxes obtained from the multiphysics simulation are also in the reported order of magnitude (Alkhudhiri et al., 2012), from 1 to 63 $\text{kg}/(\text{m}^2 \cdot \text{h})$, which were experimentally measured depending on the feed concentration, temperature, and velocity.

Fig. 8(c) and (d) show the average water and salt fluxes, respectively, with the water permeance fixed at $8 \times 10^{-7} \text{ kg}/(\text{m}^2 \cdot \text{s} \cdot \text{Pa})$ and the salt permeance varied over a range of $1 \times 10^{-10} \text{ m/s}$ to $1 \times 10^{-9} \text{ m/s}$. Salt fluxes were found to rise linearly with salt permeance, from $1.64 \times 10^{-5} \text{ kg}/(\text{m}^2 \cdot \text{hr})$ to $1.64 \times 10^{-4} \text{ kg}/(\text{m}^2 \cdot \text{hr})$, whereas water fluxes remain unchanged with varying salt permeance. Increasing salt permeance was found to negligibly affect water fluxes under the selected simulation conditions because MD membranes can achieve almost 100% rejection. In other words, even the highest salt permeance chosen in this study tended to 100% salt rejection. This can be observed from the calculated permeate concentrations shown in Fig. S2(a) and (b) in the Supporting Information, as well as the experimental results in Fig. 7. The conductivity of the permeate measured in the experiments was translated to the NaCl concentration via a calibration relation, as reported in the literature (Aldalbahi et al., 2017). Our experiments demonstrate that permeate concentrations range between $6.8 \times 10^{-5} \text{ g/L}$ and $3.67 \times 10^{-3} \text{ g/L}$ depending on the spacer type, while the computational simulations achieved 3.5×10^{-4} to $5.2 \times 10^{-3} \text{ g/L}$, which is found at the upper end of the experimental measurements. In addition, the trends of a decreasing permeate concentration with an increasing CNT content in the spacers can be related to our simulation results, demonstrating that the permeate concentration for smooth spacers is predicted to be higher

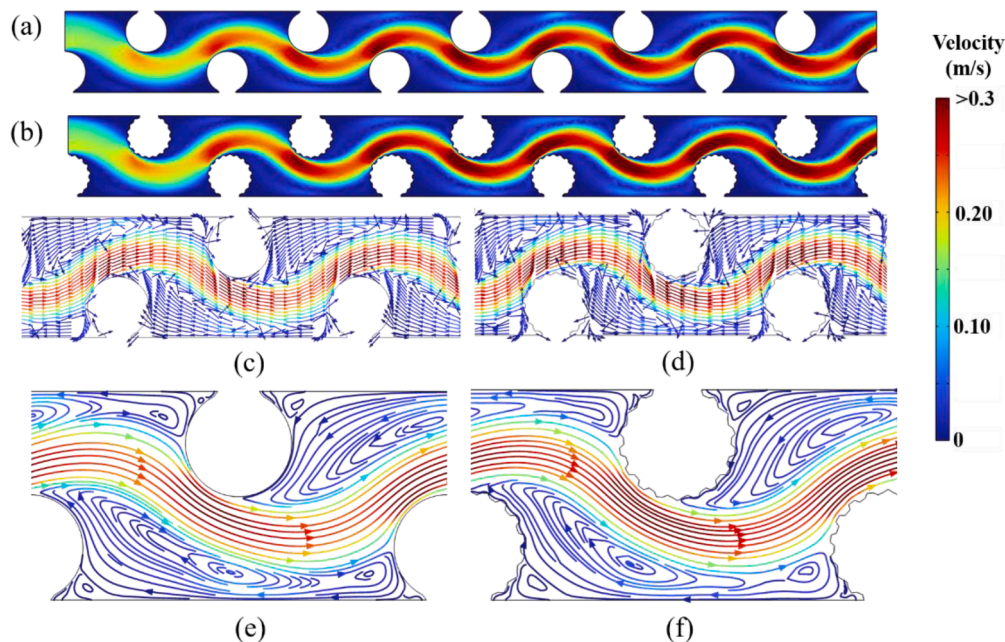


Fig. 9. Simulation results of velocity contours, vectors, and streamlines for smooth and rough spacers at a water permeance of 2×10^{-6} kg/(m²·s·Pa) and a salt permeance of 1×10^{-10} m/s. Velocity contour for (a) smooth filaments and (b) rough filaments; velocity vectors for (c) smooth filaments and (d) rough filaments; streamlines for (e) smooth filaments and (f) rough filaments.

than that for rough spacers.

Most importantly, the performances of the smooth and rough filaments were comparable in terms of water and salt fluxes. There were only negligible differences in the computed results between the two spacers. As shown in Fig. 8(a) and (c), the average water fluxes with rough filaments were higher by 0.6–1.4% than those with smooth filaments over the range of varied permeance parameters. This is qualitatively in agreement with our experimental results, where the CNT-

embedded spacers outperformed PLA spacers, although the performance disparity between the two spacers predicted by the current computational approach can be said to be almost negligible.

The present work is an initial attempt to investigate the mechanisms of flux enhancement via surface-roughness-induced micromixing in the presence of CNT-embedded spacers using a simplistic approach with several assumptions. First, the simulation domains were in 2D, and were unable to fully describe the hydrodynamics present within an actual

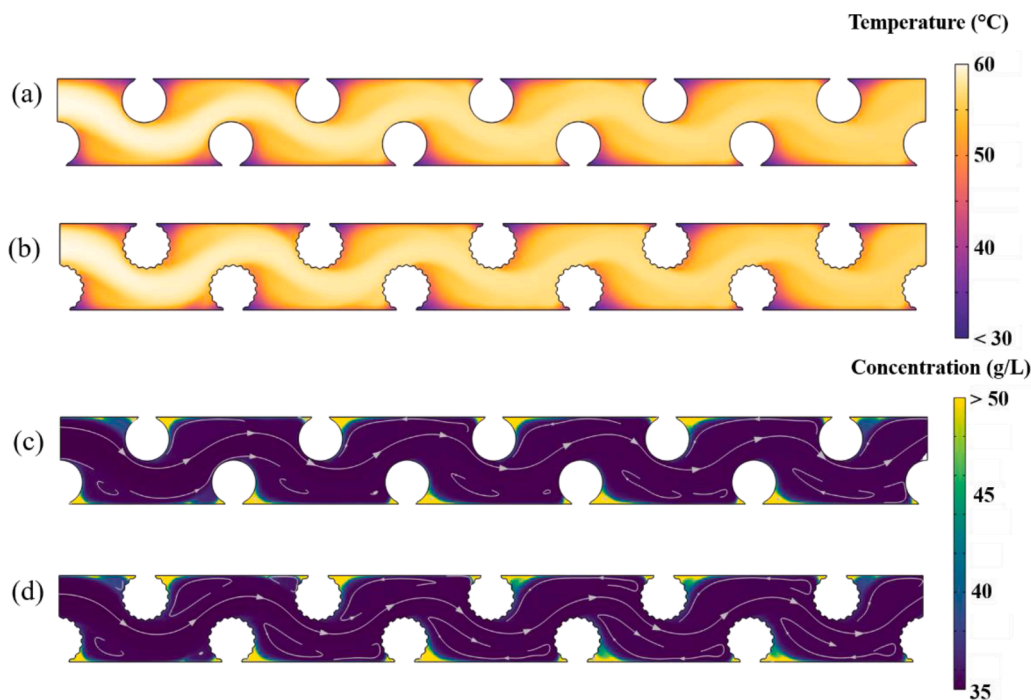


Fig. 10. Simulation results of temperature and concentration contours for smooth and rough spacers at a water permeance of 2×10^{-6} kg/(m²·s·Pa) and a salt permeance of 1×10^{-10} m/s. Temperature distributions for (a) smooth filaments and (b) rough filaments, and concentration distributions for (c) smooth filaments and (d) rough filaments.

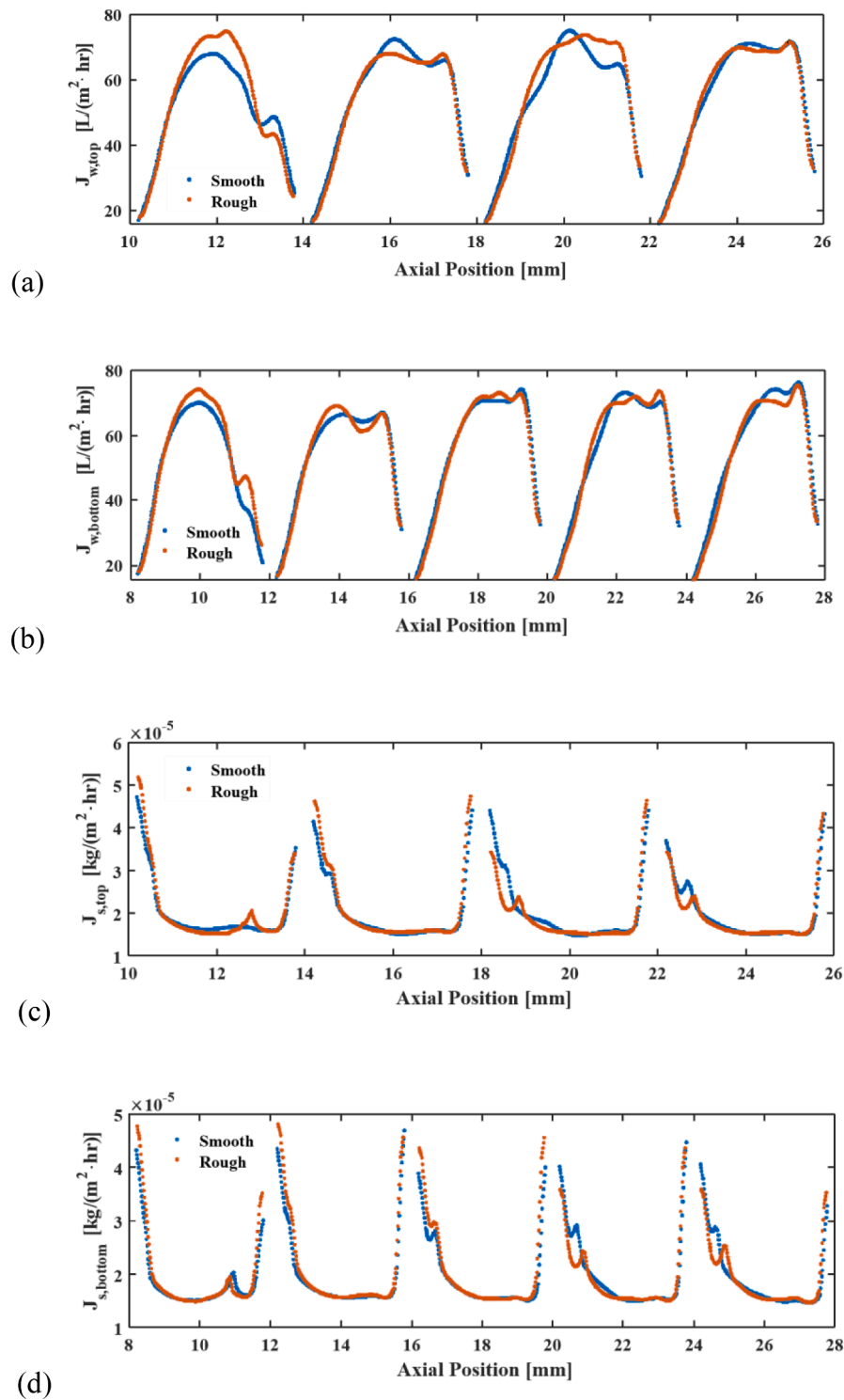


Fig. 11. Calculated water and salt fluxes through the top and bottom membranes for both smooth and rough membranes at a water permeance of 2×10^{-6} kg/(m²·s·Pa) and a salt permeance of 1×10^{-10} m/s. (a) Top water flux, (b) bottom water flux, (c) top salt flux, and (d) bottom salt flux.

spacer-filled channel. Second, the increased hydrophobicity of spacers with high CNT content was not accounted for, which could be critical in DCMD. As shown in Table 2, there was a significant jump in contact angle from 1% CNT spacer to 2% CNT spacer. Finally, the membrane material and permeate channel, which influence the calculation of heat transfer and temperature distributions, were omitted in this study. According a recent paper (Ansari et al., 2023), different shapes' detachment of spacer filaments improved the water flux and TP coefficient. In particular, CNTs are known to exhibit excellent thermal conductivity,

which may help mitigate the TP. Despite the underestimation of the performance improvement of rough spacers in multiphysics simulations, a qualitative analysis of the simulation results provides insight into the effects of surface roughness under DCMD conditions, which is discussed in the following sections.

3.4.2. Spatial distributions of flow velocity, temperature, and concentration

Fig. 9 displays velocity fields obtained from the multiphysics simulation at water permeance of 2×10^{-6} kg/(m²·s·Pa), which are almost

independent of water permeance due to the trivial value of water permeation velocity compared to bulk flow velocity (i.e., 0.064 m/s of inlet velocity vs. 1.5×10^{-5} m/s of peak permeation velocity). As shown in Fig. 9(a) and (b), the flow becomes stabilized and appears to be periodic after the fourth filament at the bottom wall. Differences in flow behaviours between smooth and rough filaments are shown in more in detail in Fig. 9(c)–(f). Both spacers accompany flow recirculation and stagnation in the areas confined by spacers and membrane walls. However, the size of flow recirculation for the two scenarios is slightly different, as shown in the velocity vector plots in Fig. 9(e) and (f): the recirculation region in the smooth filaments shown in Fig. 9(e) appears to be thinner and more stretched than that in the rough filaments. This is attributed to a more disturbed flow near the rough spacer surfaces, as shown in Fig. 10(c) and (d), which could potentially enhance fluid mixing. Furthermore, it can be expected that corrugated surfaces create tiny hollow rooms between the spacer surface and membrane walls while supporting a sheet of membranes, which could be beneficial for mitigating TP and CP.

The temperature and concentration distributions obtained from the multiphysics simulations are shown in Fig. 10. For a more distinct visualisation of TP and CP, the simulation scenario with the highest water permeance (2×10^{-6} kg/(m²·s·Pa)) was selected. Polarisation phenomena were observed in both temperature and concentration distributions, albeit to different degrees. The polarisation regions were consistent with the recirculation zones shown in Fig. 9. The minimum wall temperatures in the smooth and rough filaments were similar, at approximately 31 °C (Fig. S4 in Supporting Information). Cold spots mainly appeared in the vicinity of the spacer-membrane contact in both spacers. For concentration distributions, polarised areas had a concentration up to four times larger than the bulk concentration, that is, the wall concentration increased as high as 144 g/L near the sharp edge of the spacer-membrane contact point. Owing to the differences in micromixing that occur adjacent to the spacer surfaces, the shapes of the polarised regions were formed differently. This can be observed more clearly in the axial temperature and concentration profiles shown in Fig. S4 in the Supporting Information.

3.4.3. Water and salt fluxes along the membrane walls

The axial variations in the water and salt fluxes are presented in Fig. 11. First, the values of fluxes for both smooth and rough spacers did not differ significantly, although there are small discrepancies in peak values. Then, the trends of axial water fluxes tended to vary noticeably in each cycle, whereas the salt fluxes were rather flat. The positions of the peak water flux coincided with the lowered TP. For example, comparing Fig. 10(a) and (b) with Fig. 11(b), the back of the bottom filaments exhibited a small polarised area (higher temperature area) (Fig. 10(a)) for smooth spacers, and water flux peaks appeared at the corresponding positions (Fig. 11(b)).

Fig. 11 can be used to understand the results of average water and salt fluxes shown in Fig. 8. The predicted water and salt fluxes for smooth and rough spacers in Fig. 11(a) and (b) were approximately the same, except for minor variations near the centres of spacer filaments. The rough spacers had higher water fluxes at the first filament cycle than the smooth spacers, contributing to the higher averaged flux, as shown in Fig. 8. The shape of flux curves also indicates that the front of spacer filaments (in the positive axial direction) had aggravated TP and CP compared to the back of filaments (in the negative axial direction), which coincides with the shape of stagnation zone depicted in Fig. 9(e) and (f). Further results on concentration and temperature at the top and bottom membranes are shown in Fig. S4, which exhibited similar patterns to water and salt fluxes, respectively.

4. Conclusions

This study showed that MD performance could be improved using carbon nanofiller-embedded spacers, and that the surface roughness of

spacers could induce micromixing near the membrane surfaces via experiments and CFD simulations. The key results of this study are summarised as follows:

- In terms of MPF and IRE, spacer design has been pre-optimized to following conditions: a 45° crossing angle of the spacer filament, a 1.0 mm thickness of spacer, and a 4 mm arrangement interval of the filament.
- The surface of the carbon nanofiller-embedded spacers became a Cassie-Baxter surface and was rougher than pristine spacers. In addition, the surface roughness was found to be linked to the hydrophobicity of the spacer surface; the carbon nanofiller-embedded spacer showed a more hydrophobic surface. The highest roughness and hydrophobicity were achieved by 2% CNT spacer: WCA and roughness are $96.4 \pm 3.4^\circ$ and $64.1 \pm 8.4 \mu\text{m}$, respectively.
- The higher the surface roughness, the higher the flux. With a roughness of $64.1 \pm 8.4 \mu\text{m}$, the spacer achieved the highest MPF performance. Although carbon fillers increased the MPF, graphene did not improve the IRE, and only CNT improved the IRE performance in the MD process.
- Embedding the CNT the increased WCA on the spacer surface, and CNT spacer increased IRE from the concentration of CNT above 0.5%. The best IRE performance was achieved using the 2% CNT spacer. Further research on the IRE improvement (CP control) mechanism of CNT-embedded spacers is required.
- Preliminary CFD simulations demonstrated that flow could be more disturbed by micro-mixing in the rough spacers than in the smooth spacers, which could potentially be related to the mitigated TP and CP. These simulation results indicate that the MPF was enhanced owing to the increased surface roughness caused by CNT, which could affect the TP and CP.

Declaration of Competing Interest

The authors declare that they have no known competing financial interests or personal relationships that could have appeared to influence the work reported in this paper.

Data availability

The authors do not have permission to share data.

Acknowledgments

This research was supported by two Basic Science Research Programs through the National Research Foundation of Korea (NRF), funded by the Ministry of Education (NRF-2022R1C1C1006877 and NRF-2021R1A6A1A03039572) and by a National Research Foundation of Korea (NRF) grant funded by the Korean government (MSIT) (No. 2021R1C1C1006287).

Supplementary materials

Supplementary material associated with this article can be found, in the online version, at doi:10.1016/j.watres.2023.119649.

References

- Al-Obaidani, S., Curcio, E., Macedonio, F., Di Profio, G., Al-Hinai, H., Trioli, E., 2008. Potential of membrane distillation in seawater desalination: thermal efficiency, sensitivity study and cost estimation. *J. Membr. Sci.* 323 (1), 85–98.
- Aldabahi, A., Rahaman, M., Govindasami, P., Almoqli, M., Altalhi, T., Mezni, A., 2017. Construction of a novel three-dimensional PEDOT/RVC electrode structure for capacitive deionization: testing and performance. *Materials (Basel)* (7), 10.
- Alkhudhiri, A., Darwish, N., Hilal, N., 2012. Membrane distillation: a comprehensive review. *Desalination* 287, 2–18.

- Alsaadi, A.S., Alpatova, A., Lee, J.-G., Francis, L., Ghaffour, N., 2018. Flashed-feed VMD configuration as a novel method for eliminating temperature polarization effect and enhancing water vapor flux. *J. Membr. Sci.* 563, 175–182.
- Alsaadi, A.S., Francis, L., Amy, G.L., Ghaffour, N., 2014. Experimental and theoretical analyses of temperature polarization effect in vacuum membrane distillation. *J. Membr. Sci.* 471, 138–148.
- Ang, E.H., Tan, Y.Z., Chew, J.W., 2019. A three-dimensional plasmonic spacer enables highly efficient solar-enhanced membrane distillation of seawater. *J. Mater. Chem. A* 7 (17), 10206–10211.
- Ansari, A., Galogahi, F.M., Millar, G., Helfer, F., Thiel, D.V., Soukane, S., Ghaffour, N., 2023. Computational fluid dynamics simulations of solar-assisted, spacer-filled direct contact membrane distillation: seeking performance improvement. *Desalination* 545, 116181.
- Anvari, A., Azimi Yancheshme, A., Kekre, K.M., Ronen, A., 2020a. State-of-the-art methods for overcoming temperature polarization in membrane distillation process: a review. *J. Membr. Sci.* 616, 118413.
- Anvari, A., Kekre, K.M., Ronen, A., 2020b. Scaling mitigation in radio-frequency induction heated membrane distillation. *J. Membr. Sci.* 600, 117859.
- Attaran, M., 2017. The rise of 3-D printing: the advantages of additive manufacturing over traditional manufacturing. *Bus. Horiz.* 60 (5), 677–688.
- Bahmanyar, A., Asghari, M., Khoobi, N., 2012. Numerical simulation and theoretical study on simultaneously effects of operating parameters in direct contact membrane distillation. *Chem. Eng. Process.* 61, 42–50.
- Bogue, R., 2013. 3D printing: the dawn of a new era in manufacturing? *Assembly Autom.* 33 (4), 307–311.
- Castillo, E.H.C., Thomas, N., Al-Ketan, O., Rowshan, R., Abu Al-Rub, R.K., Nghiem, L.D., Vigneswaran, S., Arafat, H.A., Naidu, G., 2019. 3D printed spacers for organic fouling mitigation in membrane distillation. *J. Membr. Sci.* 581, 331–343.
- Chen, J.C., Li, Q., Elimelech, M., 2004. *In situ* monitoring techniques for concentration polarization and fouling phenomena in membrane filtration. *Adv. Colloid Interface Sci.* 107 (2), 83–108.
- Dongare Pratiksha, D., Alabastri, A., Pedersen, S., Zoder Katherine, R., Hogan Nathaniel, J., Neumann, O., Wu, J., Wang, T., Deshmukh, A., Elimelech, M., Li, Q., Nordlander, P., Halas Naomi, J., 2017. Nanophotonics-enabled solar membrane distillation for off-grid water purification. *Proc. Natl. Acad. Sci.* 114 (27), 6936–6941.
- Elhenawy, Y., Elminshawy, N.A.S., Bassyouni, M., Alhathal Alanezi, A., Drioli, E., 2020. Experimental and theoretical investigation of a new air gap membrane distillation module with a corrugated feed channel. *J. Membr. Sci.* 594, 117461.
- Fortunato, L., Jang, Y., Lee, J.-G., Jeong, S., Lee, S., Leiknes, T., Ghaffour, N., 2018. Fouling development in direct contact membrane distillation: non-invasive monitoring and destructive analysis. *Water Res.* 132, 34–41.
- Gurreri, L., Tamburini, A., Cipollina, A., Micale, G., Ciofalo, M., 2014. CFD prediction of concentration polarization phenomena in spacer-filled channels for reverse electrodialysis. *J. Membr. Sci.* 468, 133–148.
- Huang, Q., Gao, S., Huang, Y., Zhang, M., Xiao, C., 2019. Study on photothermal PVDF/ATO nanofiber membrane and its membrane distillation performance. *J. Membr. Sci.* 582, 203–210.
- Kharraz, J.A., Bilal, M.R., Arafat, H.A., 2015. Flux stabilization in membrane distillation desalination of seawater and brine using corrugated PVDF membranes. *J. Membr. Sci.* 495, 404–414.
- Khayet, M., Mengual, J.I., Matsuura, T., 2005. Porous hydrophobic/hydrophilic composite membranes: application in desalination using direct contact membrane distillation. *J. Membr. Sci.* 252 (1), 101–113.
- Kuang, Z., Long, R., Liu, Z., Liu, W., 2019. Analysis of temperature and concentration polarizations for performance improvement in direct contact membrane distillation. *Int. J. Heat Mass Transf.* 145, 118724.
- Kyoungjin An, A., Lee, E.J., Guo, J., Jeong, S., Lee, J.-G., Ghaffour, N., 2017. Enhanced vapor transport in membrane distillation via functionalized carbon nanotubes anchored into electrospun nanofibers. *Sci. Rep.* 7 (1), 41562.
- Lee, J.G., Jang, Y., Fortunato, L., Jeong, S., Lee, S., Leiknes, T., Ghaffour, N., 2018a. An advanced online monitoring approach to study the scaling behavior in direct contact membrane distillation. *J. Membr. Sci.* 546, 50–60.
- Lee, J.G., Jeong, S., Alsaadi, A.S., Ghaffour, N., 2018b. Influence of high range of mass transfer coefficient and convection heat transfer on direct contact membrane distillation performance. *Desalination* 426, 127–134.
- Lee, J.Y., Tan, W.S., An, J., Chua, C.K., Tang, C.Y., Fane, A.G., Chong, T.H., 2016. The potential to enhance membrane module design with 3D printing technology. *J. Membr. Sci.* 499, 480–490.
- Li, C., Zhang, J., Han, J., Yao, B., 2021. A numerical solution to the effects of surface roughness on water–coal contact angle. *Sci. Rep.* 11 (1), 459.
- Manawi, Y.M., Khraisheh, M.A.M.M., Fard, A.K., Benyahia, F., Adham, S., 2014. A predictive model for the assessment of the temperature polarization effect in direct contact membrane distillation desalination of high salinity feed. *Desalination* 341, 38–49.
- Martínez-Díez, J., Vázquez-González, M.I., 1999. Temperature and concentration polarization in membrane distillation of aqueous salt solutions. *J. Membr. Sci.* 156 (2), 265–273.
- Ngoma, M.M., Mathaba, M., Moothi, K., 2021. Effect of carbon nanotubes loading and pressure on the performance of a polyethersulfone (PES)/carbon nanotubes (CNT) membrane. *Sci. Rep.* 11 (1), 23805.
- Ni, W., Li, Y., Zhang, G., Du, X., 2022. Study of spacer structure on the enhancement of heat and mass transfer in direct contact membrane distillation modules. *Desalination* 530, 115617.
- Phattaranawik, J., Jiratananon, R., Fane, A.G., 2003. Effects of net-type spacers on heat and mass transfer in direct contact membrane distillation and comparison with ultrafiltration studies. *J. Membr. Sci.* 217 (1), 193–206.
- Politano, A., Argurio, P., Di Profio, G., Sanna, V., Cupolillo, A., Chakraborty, S., Arafat, H.A., Curcio, E., 2017. Photothermal membrane distillation for seawater desalination. *Adv. Mater.* 29 (2).
- Politano, A., Di Profio, G., Fontananova, E., Sanna, V., Cupolillo, A., Curcio, E., 2019. Overcoming temperature polarization in membrane distillation by thermoplasmonic effects activated by Ag nanofillers in polymeric membranes. *Desalination* 451, 192–199.
- Ragunath, S., Roy, S., Mitra, S., 2018. Carbon nanotube immobilized membrane with controlled nanotube incorporation via phase inversion polymerization for membrane distillation based desalination. *Sep. Purif. Technol.* 194, 249–255.
- Ramiasa, M., Ralston, J., Fetzter, R., Sedev, R., 2014. The influence of topography on dynamic wetting. *Adv. Colloid Interface Sci.* 206, 275–293.
- Shukla, S., Méricq, J.P., Belleville, M.P., Hengl, N., Benes, N.E., Vankelecom, I., Sanchez Marcano, J., 2018. Process intensification by coupling the Joule effect with pervaporation and sweeping gas membrane distillation. *J. Membr. Sci.* 545, 150–157.
- Siddiqui, A., Farhat, N., Bucs, S.S., Linares, R.V., Picioreanu, C., Kruithof, J.C., van Loosdrecht, M.C., Kidwell, J., Vrouwenvelder, J.S., 2016. Development and characterization of 3D-printed feed spacers for spiral wound membrane systems. *Water Res.* 91, 55–67.
- Taamneh, Y., Bataineh, K., 2017. Improving the performance of direct contact membrane distillation utilizing spacer-filled channel. *Desalination* 408, 25–35.
- Tan, Y.Z., Ang, E.H., Chew, J.W., 2019. Metallic spacers to enhance membrane distillation. *J. Membr. Sci.* 572, 171–183.
- Thomas, N., Kumar, M., Palmisano, G., Al-Rub, R.K.A., Alnuaimi, R.Y., Alhseinat, E., Rowshan, R., Arafat, H.A., 2021a. Antiscalant 3D printed feed spacers via facile nanoparticle coating for membrane distillation. *Water Res.* 189, 116649.
- Thomas, N., Mavukkandy, M.O., Loutatidou, S., Arafat, H.A., 2017. Membrane distillation research & implementation: lessons from the past five decades. *Sep. Purif. Technol.* 189, 108–127.
- Thomas, N., Sreedhar, N., Al-Ketan, O., Rowshan, R., Abu Al-Rub, R.K., Arafat, H., 2018. 3D printed triply periodic minimal surfaces as spacers for enhanced heat and mass transfer in membrane distillation. *Desalination* 443, 256–271.
- Thomas, N., Sreedhar, N., Al-Ketan, O., Rowshan, R., Abu Al-Rub, R.K., Arafat, H., 2019. 3D printed spacers based on TPMS architectures for scaling control in membrane distillation. *J. Membr. Sci.* 581, 38–49.
- Thomas, N., Swaminathan, J., Zaragoza, G., Abu Al-Rub, R.K., Lienhard V, J.H., Arafat, H.A., 2021b. Comparative assessment of the effects of 3D printed feed spacers on process performance in MD systems. *Desalination* 503.
- Tijing, L.D., Dizon, J.R.C., Ibrahim, I., Nisay, A.R.N., Shon, H.K., Advincula, R.C., 2020. 3D printing for membrane separation, desalination and water treatment. *Appl. Mater. Today* 18.
- Ve, Q.L., Koirala, R., Bawahab, M., Faqeha, H., Do, M.C., Nguyen, Q.L., Date, A., Akbarzadeh, A., 2021. Experimental investigation of the effect of the spacer and operating conditions on mass transfer in direct contact membrane distillation. *Desalination* 500, 114839.
- Wang, J., Wu, Y., Cao, Y., Li, G., Liao, Y., 2020. Influence of surface roughness on contact angle hysteresis and spreading work. *Colloid Polym. Sci.* 298 (8), 1107–1112.
- Ye, H., Li, X., Deng, L., Li, P., Zhang, T., Wang, X., Hsiao, B.S., 2019. Silver nanoparticle-enabled photothermal nanofibrous membrane for light-driven membrane distillation. *Ind. Eng. Chem. Res.* 58 (8), 3269–3281.